Synthesis of Fe_3O_4/Hydroxyapatite Nanocomposites: Structural, Surface, and Magnetic Characterization

Ahmad Fadli[1], Agung Prabowo[2*], Drastinawati Drastinawati[1], Bima Wandika Putra[1], Heni Sugesti[3], and Febriyati Puspasari[2]

[1]*Department of Chemical Engineering, Faculty of Engineering, Universitas Riau, Kampus Binawidya, Jl. HR. Soebrantas Km. 12.5, Simpang Baru, Panam Pekanbaru, Riau 28293, Indonesia*

[2]*Department of Chemical Engineering, Politeknik Negeri Samarinda, Jl. Dr. Cipto Mangunkusumo, Samarinda 75131, Indonesia*

[3]*Department of Chemical Engineering, Politeknik Negeri Sriwijaya, Jl. Srijaya Negara Bukit Besar, Palembang 30139, Indonesia*

* ***Corresponding author:***

email: agungprabowo@polnes.ac.id

Received: June 9, 2025
Accepted: September 26, 2025

DOI: 10.22146/ijc.107697

Abstract: *Magnetite/hydroxyapatite (Fe_3O_4/HA) nanocomposites are promising materials for biomedical applications, particularly in targeted drug delivery. This study investigates the effects of hydrothermal reaction time and $FeCl_3$ precursor concentration on the structural, morphological, and magnetic properties of Fe_3O_4/HA composite powders synthesized via a one-pot hydrothermal method. The resulting composites exhibit biphasic structures comprising magnetite (cubic phase) and hydroxyapatite (hexagonal phase) crystallites, with average sizes ranging from 22 to 30 nm. Both increased reaction time and $FeCl_3$ concentration contributed to the growth of crystal size. A notable enhancement in specific surface area was observed, increasing from 48.21 to 67.41 m^2/g as $FeCl_3$ concentration decreased from 0.15 to 0.05 M at a fixed reaction time of 15 h. Magnetic characterization revealed that the composites exhibited superparamagnetic behavior, with the highest saturation magnetization (Ms) reaching 17.27 emu/g. These results demonstrate that tuning synthesis parameters can optimize the structural and magnetic properties of Fe_3O_4/HA nanocomposites, making them strong candidates for use in controlled drug delivery systems.*

Keywords: *composite; drug delivery; hydrothermal; hydroxyapatite; magnetite*

■ INTRODUCTION

Magnetic nanoparticles, particularly magnetite (Fe_3O_4), have garnered significant attention in recent years due to their distinctive superparamagnetic properties, nanoscale size, and inherent biocompatibility. These features make them highly attractive for various biomedical applications, including magnetic resonance imaging (MRI) as contrast agents, magnetic hyperthermia for localized cancer therapy, and targeted drug delivery systems [1-2]. Among these, drug delivery is one of the most promising applications, where Fe_3O_4 nanoparticles can be guided to specific sites in the body using an external magnetic field, enabling localized drug release. This targeted approach helps to minimize systemic side effects, reduce required dosages, and enhance overall therapeutic efficacy [3-5].

Despite these advantages, the clinical and practical use of bare Fe_3O_4 nanoparticles is hindered by several critical limitations. These include a tendency to aggregate due to high surface energy, susceptibility to rapid clearance by the reticuloendothelial system (RES), and instability under physiological conditions. Moreover, they often exhibit burst release behaviors, which can lead to uncontrolled drug distribution and reduced therapeutic efficiency [6-8]. These issues necessitate the development of surface modification strategies to improve the colloidal stability, biocompatibility, and functionality of Fe_3O_4 nanoparticles in biological environments. To address these challenges, a wide range of surface coatings has been explored. Polymeric coatings, such as polyethylene

glycol (PEG), dextran, and polyvinyl alcohol, are among the most used due to their hydrophilic nature, which helps prevent aggregation and reduces protein adsorption (biofouling) [9-11]. However, many of these organic polymers are prone to degradation under physiological conditions, limiting their long-term effectiveness and structural integrity [12-14].

In contrast, inorganic coatings, particularly hydroxyapatite (HA, $Ca_{10}(PO_4)_6(OH)_2$), offer a more stable and bioactive alternative. HA is the primary inorganic component of natural bone and teeth, and it is well known for its outstanding biocompatibility, osteoconductivity, and bioactivity. These properties make it especially suitable for bone-related drug delivery and regenerative medicine applications [15-17]. Moreover, when Fe_3O_4 nanoparticles are incorporated into an HA matrix, the resulting composites retain the magnetic functionality of Fe_3O_4 while leveraging the biological advantages of HA. This composite approach has been shown to improve nanoparticle dispersion, control particle morphology, and reduce toxicity, while maintaining the chemical stability of HA [18-19].

The method of synthesis also plays a critical role in determining the structural and functional characteristics of these nanocomposites. Among the available techniques, hydrothermal synthesis has emerged as a particularly effective route due to its ability to produce highly crystalline, phase-pure materials with tunable morphology and particle size [20]. For example, Puthumana and Rahul [21] successfully synthesized Fe_3O_4/HA nanocomposites using a hydrothermal approach, achieving uniform particle dispersion and demonstrating favorable drug adsorption and sustained release profiles for model therapeutic agents. Building on these findings, the present study aims to synthesize Fe_3O_4/HA nanocomposites via a one-pot hydrothermal process while systematically varying the hydrothermal reaction time and $FeCl_3$ precursor concentration. Unlike previous studies that primarily demonstrated the feasibility of Fe_3O_4/HA composites for drug delivery, this work provides a comprehensive investigation of how these synthesis parameters influence the structural, morphological, surface, and magnetic properties of the composites. By explicitly linking synthesis conditions with functional characteristics relevant to drug delivery, this study offers new insights into tailoring Fe_3O_4/HA nanocomposites for enhanced biomedical performance.

■ EXPERIMENTAL SECTION

Materials

In this study, the chemicals used included $FeCl_3{\cdot}6H_2O$ (Merck), distilled water, urea (Merck), sodium citrate dihydrate ($C_6H_5O_7Na_3{\cdot}2H_2O$, Merck), polyethylene glycol (PEG 1000, 99%, Merck), ethanol (98%, Merck), and HA (Merck).

Instrumentation

The structure and crystal phase of the Fe_3O_4/HA composites were characterized by X-ray diffraction (XRD) using a PANalytical X'Pert Powder diffractometer with a copper (Cu) anode operated at 30 mA and 40 kV. XRD data were collected at 300 K over a range of Bragg angles (2θ). The specific surface area of the composites was measured using a Brunauer–Emmett–Teller (BET) analyzer (Nova 3200e). Magnetic properties were evaluated using a vibrating sample magnetometer (VSM-250 electromagnet) at 300 K, under an applied magnetic field ranging from −20 to +20 kOe. The morphology of the Fe_3O_4/HA composites was examined using transmission electron microscopy (TEM, JEM-1400).

Procedure

Fe_3O_4/HA composites were synthesized using a hydrothermal method. A solution containing 2 mmol of $FeCl_3{\cdot}6H_2O$, 4 mmol of $Ca(NO_3)_2{\cdot}4H_2O$, and 6 mmol of urea was prepared by dissolving the reagents in 40 mL of distilled water. The $Ca(NO_3)_2{\cdot}4H_2O$ was used as the calcium source, which, under hydrothermal conditions, reacts with phosphate groups to facilitate the formation of HA crystals. Subsequently, 0.3 g of PEG (7.5 g/L) was added under continuous stirring until fully dissolved. HA was then added at 30 wt.% relative to the total solid content.

The resulting solution was transferred into a 100 mL Teflon-lined stainless-steel autoclave, which was then placed in an oven and heated at 210 °C for various

durations (5, 7, 9, 12, and 15 h) with $FeCl_3$ concentrations of 0.05, 0.10, and 0.15 M. After the reaction, the autoclave was allowed to cool naturally to room temperature. The dark brown precipitate was collected by centrifugation, washed several times with distilled water and absolute ethanol, and dried in an oven at 110 °C for 12 h. All syntheses were conducted at a constant temperature of 210 °C.

■ RESULTS AND DISCUSSION

XRD

The effect of hydrothermal reaction time on the crystallinity of Fe_3O_4/HA composites is clearly demonstrated in the XRD patterns shown in Fig. 1. A progressive enhancement in crystallinity is observed as the reaction time increases from 5 to 15 h. Among all samples, the one synthesized at 15 h exhibited the most intense and well-defined diffraction peaks, indicative of high crystallinity and improved phase purity. Conversely, the sample synthesized for only 5 h displayed significantly broader and less intense peaks, suggesting the presence of poorly crystalline or partially developed phases. The intermediate samples (7, 9, and 12 h) showed a gradual transition in peak sharpness and intensity, highlighting the importance of thermal treatment duration in promoting complete crystallite formation.

Of particular importance are the distinct peaks at 2θ ≈ 31.7° and 35.5°, which correspond to the (211) plane of HA and the (311) plane of Fe_3O_4, respectively. These peaks became increasingly sharper and more intense with extended reaction time, indicating that both HA and Fe_3O_4 phases benefited from prolonged thermal energy input during the hydrothermal synthesis process. This trend is consistent with classical crystal growth theories, which suggest that longer reaction durations enable greater atomic mobility and improved crystallite ordering, resulting in more defined lattice structures. The findings agree with recent studies showing that longer hydrothermal times significantly improve the phase purity and crystallinity of iron oxide-ceramic nanocomposites.

The influence of $FeCl_3$ concentration on phase formation is presented in Fig. 2. As the concentration of the Fe^{3+} precursor increased from 0.05 to 0.15 M, a noticeable intensification and sharpening of XRD peaks was observed. The sample synthesized with 0.15 M $FeCl_3$ displayed the most prominent reflections, indicating the formation of well-ordered Fe_3O_4 and HA phases. In contrast, the lower concentration samples (0.05 and 0.10 M) showed less intense peaks, suggesting either

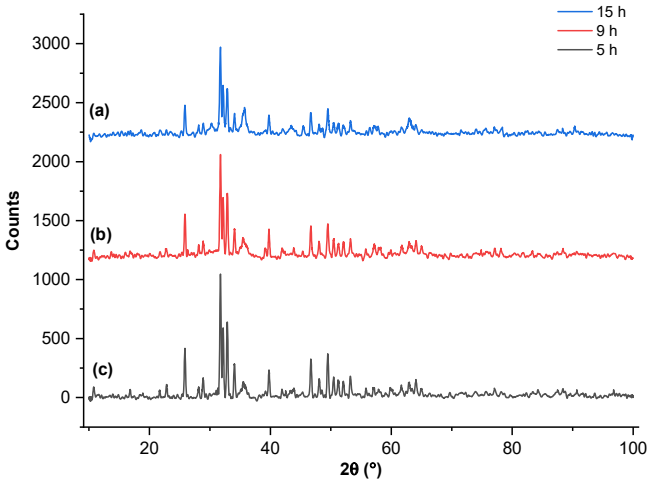

Fig 1. XRD patterns of Fe_3O_4/HA nanocomposites prepared via hydrothermal synthesis at different reaction times: (a) 15 h, (b) 9 h, and (c) 5 h. The patterns indicate the phase evolution and crystallinity changes with increasing synthesis duration

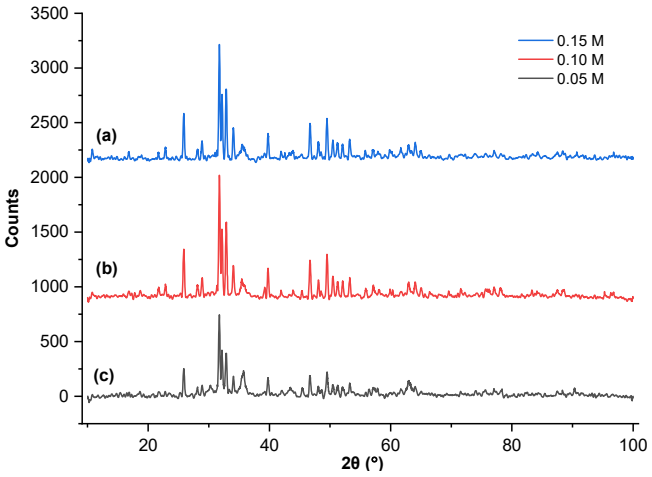

Fig 2. XRD patterns of Fe_3O_4/HA nanocomposites synthesized via hydrothermal method using different concentrations of $FeCl_3$ precursor: (a) 0.15 M, (b) 0.10 M, and (c) 0.05 M. The patterns reflect changes in phase composition and crystallinity as a function of iron precursor concentration

incomplete nucleation or the presence of amorphous intermediates. Higher Fe^{3+} concentrations likely promote a greater number of nucleation sites during hydrothermal processing, enhancing the growth kinetics and leading to more uniform and crystalline product phases.

The synergy between reaction time and $FeCl_3$ concentration is therefore critical in governing the final crystalline quality of Fe_3O_4/HA nanocomposites. Enhanced crystallinity is highly beneficial for biomedical applications, particularly in drug delivery and bone regeneration, as it influences mechanical integrity, phase stability, and the interaction of the material with biological fluids. Well-crystallized HA ensures better bioactivity and osteoconductivity, while crystalline Fe_3O_4 improves magnetic responsiveness and structural uniformity, both of which are essential for consistent performance in magnetically guided drug delivery systems. In conclusion, both extended hydrothermal reaction time and elevated $FeCl_3$ concentration significantly enhance the crystalline structure and phase development of Fe_3O_4/HA nanocomposites. These findings underscore the importance of optimizing synthesis parameters to achieve materials with desirable physicochemical properties for biomedical deployment.

The XRD patterns of the Fe_3O_4/HA nanocomposites synthesized under varying hydrothermal reaction times are presented in Fig. 1. Distinct diffraction peaks at $2\theta \approx 31.7°$ (HA, (211) plane) and 35.5° (Fe_3O_4, (311) plane) became sharper and more intense with increasing reaction time. The sample synthesized at 15 h exhibited the highest peak intensities, while the lowest were observed for the 5 h sample. These results indicate that extended hydrothermal treatment enhances crystallinity by facilitating more complete nucleation and crystal growth. Fig. 2 displays the XRD patterns of samples synthesized with varying $FeCl_3$ concentrations. Similar to the time-dependent behavior, the peak intensities increased with higher precursor concentrations. The most intense diffraction peaks were observed for the composite prepared at 0.15 M $FeCl_3$, followed by 0.10 and 0.05 M. These results suggest that higher Fe^{3+} ion availability promotes more efficient nucleation and crystallite formation, thereby enhancing the overall crystallinity of the Fe_3O_4/HA composite.

The average crystallite size of the Fe_3O_4 and HA phases was estimated from the X-ray diffraction data using the Scherrer equation (Eq. (1)):

$$D = \frac{K\lambda}{\beta \cos\theta} \quad (1)$$

where D is the crystallite size (nm), K is the shape factor (commonly taken as 0.9), λ is the X-ray wavelength (0.1541 nm for Cu Kα radiation), β is the full width at half maximum (FWHM) of the selected diffraction peak (in radians), and θ is the Bragg diffraction angle (in degrees). The estimated crystallite sizes of both Fe_3O_4 and HA phases at various hydrothermal reaction times are summarized in Table 1.

The data presented in Table 1 indicate that both reaction time and $FeCl_3$ concentration significantly influence the crystallite size of the Fe_3O_4/HA composites. Prolonging the hydrothermal reaction time resulted in an increase in crystallite size from 12.94 nm at 5 h to 22.77 nm at 15 h. This trend suggests that longer reaction durations promote crystal growth and grain coarsening. Additionally, increasing the $FeCl_3$ concentration was found to affect crystal morphology; higher reactant concentrations led to more distorted particle shapes and

Table 1. Crystallite size of Fe_3O_4/HA composites under different synthesis conditions

Concentration of $FeCl_3$ (M)	Reaction time (h)	Crystal size (nm)	
		Magnetite	Hydroxyapatite
0.05	5	12.94	16.71
	7	14.75	18.89
	9	14.90	20.64
	12	15.31	22.24
	15	18.41	22.61
0.10	5	14.40	18.39
	7	15.67	20.12
	9	16.12	21.40
	12	18.21	22.68
	15	19.71	24.05
0.15	5	16.61	20.61
	7	17.49	21.28
	9	18.70	23.59
	12	20.78	24.21
	15	22.77	30.31

coarser grain sizes [22-24]. The crystal growth behavior of Fe_3O_4 particles synthesized via hydrothermal methods is strongly influenced by reaction time and precursor concentration. In this study, the increasing reaction time promoted larger crystal diameters, which is consistent with the oriented attachment mechanism previously described by Fadli et al. [25], where small primary Fe_3O_4 nanocrystals align and fuse along specific crystallographic orientations to form larger, single-domain crystals. Overall, the composite crystallite sizes obtained in this study remain within the nanometer range, confirming the successful synthesis of nanoscale Fe_3O_4/HA composites with controlled crystal growth.

The synthesis was conducted at a constant temperature of 210 °C, with variations in reaction time and $FeCl_3$ concentration. Crystallite sizes of both Fe_3O_4 and HA were calculated from XRD data using the Scherrer equation. At a $FeCl_3$ concentration of 0.05 M and a reaction time of 5 h, the crystallite sizes of Fe_3O_4 and HA were 12.94 and 16.71 nm, respectively. As the reaction time increased, a progressive growth in crystallite size was observed: 14.75 and 18.89 nm at 7 h, 14.90 and 20.64 nm at 9 h, 15.31 and 22.24 nm at 12 h, and finally 18.41 and 22.61 nm at 15 h for Fe_3O_4 and HA, respectively. The enlargement of HA crystallite size with increasing reaction time can be explained by the progressive crystal growth and Ostwald ripening phenomena under prolonged hydrothermal conditions, allowing smaller crystallites to dissolve and redeposit onto larger ones. In addition, the presence of higher Fe ion concentrations enhances supersaturation, providing additional driving force for crystal growth. Fe ions may also interact with the HA lattice, either through partial substitution or surface adsorption, thereby stabilizing larger crystallites. Together, these effects explain the increase in crystallite size observed at extended reaction times and elevated Fe concentrations.

Similar trends were observed for $FeCl_3$ concentrations of 0.10 and 0.15 M, where crystallite sizes also increased with extended reaction time, albeit with slight fluctuations. These minor deviations may be attributed to the dynamic chemical environment during the hydrothermal process [26]. In particular, the presence of citrate ions may have contributed to partial reduction or complexation effects, potentially affecting particle stability and resulting in temporary decreases in crystal size. Nonetheless, the formation of Fe_3O_4/HA nanocomposites with crystallite sizes in the nanometer range was successfully achieved under all synthesis conditions.

TEM Analysis

The morphology of the synthesized Fe_3O_4/HA composites was examined using TEM, as shown in Fig. 3. The sample synthesized with a reaction time of 15 h and an $FeCl_3$ concentration of 0.15 M exhibited a granular morphology composed of uniformly dispersed nanoscale particles. The particle size distribution ranged from 10 to 30 nm, with an average diameter of approximately 15 nm. Such morphology reflects the influence of synthesis parameters on nucleation and growth kinetics. A longer hydrothermal treatment promotes sustained crystal growth and allows nanoparticles to reach thermodynamically stable morphologies [27-28]. Meanwhile, higher $FeCl_3$ concentrations provide more Fe^{3+} ions, facilitating uniform nucleation and preventing excessive agglomeration. The absence of large aggregates and the homogeneous particle distribution suggest that the reaction conditions were effective in producing nanocomposites with controlled grain size and dispersion, consistent with previous reports on Fe_3O_4-ceramic systems [29-31]. For biomedical applications,

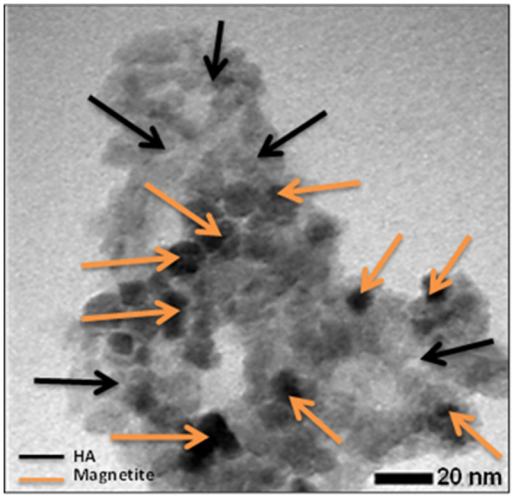

Fig 3. TEM image of the sample synthesized at 210 °C for 12 h with a magnification of 150,000×

particularly drug delivery, particle uniformity in both shape and size is crucial. Uniform nanoscale morphology enhances the physicochemical stability and functionality of the composite. A well-defined and consistent particle size increases the specific surface area, thereby improving the composite's efficiency in drug adsorption and controlled release [32-34]. The observed morphology confirms the potential suitability of the synthesized Fe_3O_4/HA nanocomposites for drug delivery systems.

According to Zheltova et al. [9], regions of darker contrast in TEM images are indicative of Fe_3O_4 cores, whereas lighter regions correspond to the HA component. The presence of a darker core encapsulated by a lighter outer shell suggests that Fe_3O_4 nanoparticles are uniformly coated by a HA layer. This core–shell configuration implies successful surface functionalization of Fe_3O_4 by HA during the hydrothermal synthesis process. As illustrated in Fig. 3, the composite particles exhibit a predominantly spherical morphology, with Fe_3O_4 cores visibly embedded within the surrounding HA matrix. This encapsulation is critical for biomedical applications, as it not only enhances biocompatibility but also helps to prevent agglomeration of the magnetic cores, thereby preserving their superparamagnetic properties for targeted drug delivery.

BET Analysis

The specific surface areas of the synthesized Fe_3O_4/HA nanocomposites, determined using nitrogen adsorption–desorption isotherms and calculated via the BET method, are summarized in Table 2. A clear and consistent trend was observed wherein increasing the concentration of $FeCl_3$ precursor led to a significant increase in the surface area of the resulting composites, while the hydrothermal reaction conditions, specifically temperature and time (180 °C for 15 h), were kept constant. Notably, the composite synthesized with 0.05 M $FeCl_3$ exhibited a surface area of 48.21 m^2/g, whereas increasing the $FeCl_3$ concentration to 0.15 M resulted in a surface area of 67.41 m^2/g. This enhancement is primarily attributed to the formation of finer Fe_3O_4 nanoparticles and a more porous microstructure within the HA matrix at higher Fe^{3+} concentrations.

Table 2. Specific surface area of Fe_3O_4/HA

Sample reaction time (h)	Concentration of $FeCl_3$ (M)	Specific surface area (m^2/g)
5	0.05	48.21
9	0.10	64.48
15	0.15	67.41

The BET surface area data show a strong inverse relationship with crystallite size, as determined by XRD analysis using the Scherrer equation. Smaller crystallite sizes result in broader diffraction peaks, indicating a larger specific surface area due to the increased number of active sites per unit mass. With increasing $FeCl_3$ concentration, the higher nucleation rate of Fe_3O_4 particles likely leads to a finer dispersion and a greater number of nucleation centers, which in turn limit crystal growth and reduce particle size. As demonstrated in similar studies, the formation of ultrasmall Fe_3O_4 crystallites within or on HA frameworks results in increased porosity and a higher external surface area available for functional interactions [28].

This microstructural refinement, driven by precursor concentration, significantly affects the physicochemical properties of the composites. The increased surface area enhances the materials' potential in biomedical applications, particularly in the context of drug delivery systems [35-36]. High surface area materials are advantageous for drug adsorption because they provide more available surface functional groups—such as hydroxyl, phosphate, and iron oxide sites—which can interact with drug molecules through hydrogen bonding, van der Waals forces, or electrostatic interactions [37-38]. Moreover, the presence of Fe_3O_4 imparts magnetic responsiveness to the composite, allowing for external magnetic guidance and site-specific targeting, a key feature in modern targeted drug delivery strategies. Furthermore, HA serves not only as a biocompatible scaffold but also as a pH-sensitive matrix that can aid in the controlled release of drugs in targeted environments such as tumor tissues, which typically exhibit acidic microenvironments. When integrated with magnetically active Fe_3O_4, the composite can be fine-tuned to deliver dual functionality: magnetic targeting and pH-triggered release. These synergistic

effects make Fe_3O_4/HA nanocomposites an attractive platform for multifunctional therapeutic applications.

In conclusion, the increase in BET surface area with $FeCl_3$ concentration highlights the importance of synthesis conditions in tuning the structural properties of Fe_3O_4/HA composites. This structural modulation has direct implications for optimizing the drug loading and release efficiency of the material, underlining its potential utility in advanced drug delivery systems. The specific surface area of the Fe_3O_4/HA composites obtained in this study ranged from 48.21 to 67.41 m^2/g. These values are notably higher than those reported by Nakahira and Sato [39], indicating improved surface characteristics of the synthesized materials. In the context of drug delivery applications, surface area plays a crucial role in determining the loading and release efficiency of therapeutic agents. A higher specific surface area provides more active sites for drug adsorption, thereby enhancing the composite's drug-carrying capacity and improving the overall performance of the delivery system.

Analysis of Vibrating Sample Magnetometer (VSM)

The magnetic properties of the Fe_3O_4/HA composites were characterized using a vibrating sample magnetometer (VSM) at room temperature under an applied magnetic field ranging from –20 to +20 kOe. The resulting hysteresis loops for the samples are presented in Fig. 4. The saturation magnetization (Ms) values varied significantly as a function of $FeCl_3$ precursor concentration, revealing a concentration-dependent magnetic response. Notably, the sample synthesized with 0.05 M $FeCl_3$ displayed the highest Ms value of 17.27 emu/g, while the composite prepared using 0.15 M $FeCl_3$ exhibited a lower Ms value of 13.24 emu/g. These values reflect the magnetic contribution of Fe_3O_4 within the composite matrix, and the observed decrease in Ms with increasing $FeCl_3$ concentration suggests a complex interplay between magnetic phase distribution, crystallinity, and interparticle interactions. The inverse trend between $FeCl_3$ concentration and Ms is somewhat counterintuitive, as one might initially expect higher precursor concentrations to result in greater Fe_3O_4 content and therefore increased magnetization. However, this reduction in Ms is consistent with XRD results, which indicate a decrease in crystallinity at higher $FeCl_3$ concentrations. The broadening and reduction of XRD peak intensities suggest that at elevated Fe^{3+} concentrations, Fe_3O_4 nanoparticles may form with poorer crystalline order or increased lattice defects, which disrupt the alignment of magnetic domains and reduce net magnetization [28].

Furthermore, high precursor concentrations may also promote agglomeration or non-uniform growth of Fe_3O_4 nanoparticles, which can lead to enhanced surface spin disorder and superparamagnetic behavior, both of which contribute to a decrease in saturation magnetization [40]. Surface spin canting, where surface atoms experience a disordered spin alignment due to unsaturated bonds or structural imperfections, is particularly significant in nanoparticles with high surface-to-volume ratios. These effects are exacerbated when Fe_3O_4 particles are embedded within an HA matrix, as the interface may further perturb the magnetic order, depending on the surface chemistry and synthesis conditions [41].

From a biomedical standpoint, particularly in targeted drug delivery and magnetic hyperthermia, the

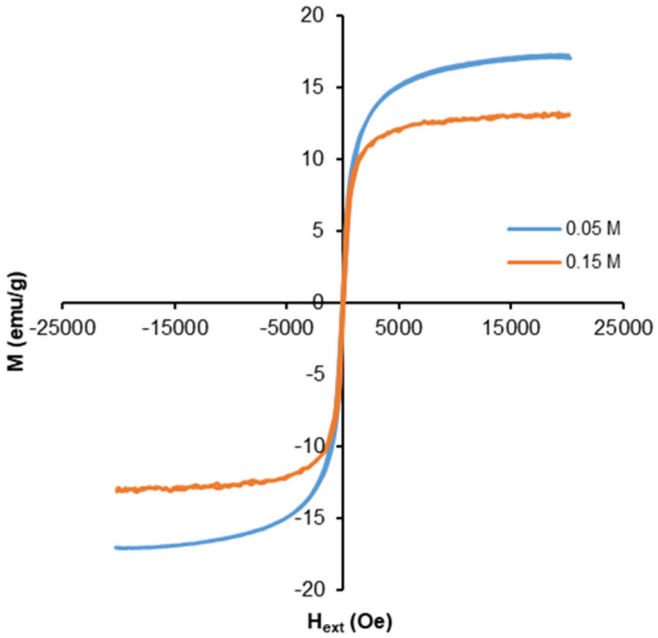

Fig 4. Hysteresis curve of Fe_3O_4/HA composite synthesized by comparison of Fe_3O_4/HA 15 h at concentration $FeCl_3$ of 0.05 M

magnetic properties of nanocomposites play a central role. Materials with moderate saturation magnetization—typically in the range of 10–30 emu/g—are ideal for external magnetic guidance without causing particle aggregation under physiological conditions [42]. In this context, the Ms values observed for all Fe_3O_4/HA samples in this study fall within the suitable range for magnetically responsive drug delivery, offering an effective balance between magnetic responsiveness and colloidal stability. Moreover, maintaining biocompatibility is essential, and HA provides an excellent platform for improving the osteoconductivity and cytocompatibility of the composite. The decline in magnetization at higher $FeCl_3$ concentrations may also be linked to an increased HA-to-Fe_3O_4 ratio in the matrix, which dilutes the magnetic phase and further lowers the composite's overall Ms.

In summary, the magnetic characterization of Fe_3O_4/HA nanocomposites reveals a clear inverse relationship between $FeCl_3$ precursor concentration and saturation magnetization. The optimal balance between crystallinity, particle uniformity, and magnetic response was achieved at a concentration of 0.05 M $FeCl_3$, synthesized over 15 h, making it a promising candidate for magnetically guided biomedical applications. The coercivity (Hc) values also differed between samples, with the composite synthesized at 0.05 M $FeCl_3$ exhibiting a coercivity of 84.43 Oe, and the one synthesized at 0.15 M $FeCl_3$ showing a higher coercivity of 101.78 Oe. These values indicate that the composites retain superparamagnetic behavior at room temperature, which is typical for Fe_3O_4 particles with sizes below 30 nm [9]. The variation in coercivity is primarily attributed to particle size, as larger particles tend to exhibit higher coercivity due to the increased magnetic anisotropy energy required to realign their magnetic domains. Therefore, the lower coercivity observed at 0.05 M may be linked to finer particle sizes and higher crystallinity, as supported by the structural characterization results.

■ CONCLUSION

In this study, Fe_3O_4/HA nanocomposites were successfully synthesized via the hydrothermal method. The resulting composites exhibited superparamagnetic behavior and consisted of well-dispersed nanoparticles with average crystallite sizes of approximately 15 nm for Fe_3O_4 and 25 nm for HA, as confirmed by XRD and TEM analyses. The morphology analysis revealed a uniform size distribution with minimal agglomeration, and Fe_3O_4 nanoparticles were homogeneously distributed on the HA matrix. The combination of nanoscale particle size, high crystallinity, and superparamagnetic properties indicates that the synthesized Fe_3O_4/HA composites hold significant promise for biomedical applications. These include targeted drug delivery, magnetic hyperthermia for cancer therapy, and other magnetically assisted medical treatments.

■ ACKNOWLEDGMENTS

The authors gratefully acknowledge the support provided by Biomaterial Research Group, Chemical Engineering of Universitas Riau and Chemical Engineering Department of Politeknik Negeri Samarinda.

■ CONFLICT OF INTEREST

The authors declare no conflict of interest.

■ AUTHOR CONTRIBUTIONS

Ahmad Fadli contributed to the conceptualization, methodology development, investigation and formal analysis. Agung Prabowo participated in the conceptualization, writing of the original draft, supervision, and review and editing of the manuscript. Drastinawati was involved in conceptualization, supervision, and manuscript review and editing. Bima Wandika Putra contributed to the conceptualization, supervision, and formal analysis. Heni Sugesti contributed to the review and editing of the manuscript. Febriyati Puspasari contributed to conceptualization and editing of the manuscript.

■ REFERENCES

[1] Kaczmarek, K., Mrówczyński, R., Hornowski, T., Bielas, R., and Józefczak, A., 2019, The effect of tissue-mimicking phantom compressibility on magnetic hyperthermia, *Nanomaterials*, 9 (5), 803.

[2] Obaidat, I.M., Narayanaswamy, V., Alaabed, S., Sambasivam, S., and Muralee Gopi, C.V., 2019, Principles of magnetic hyperthermia: A focus on

using multifunctional hybrid magnetic nanoparticles, *Magnetochemistry*, 5 (4), 67.

[3] Islam, K., Haque, M., Kumar, A., Hoq, A., Hyder, F., and Hoque, S.M., 2020, Manganese ferrite nanoparticles ($MnFe_2O_4$): Size dependence for hyperthermia and negative/positive contrast enhancement in MRI, *Nanomaterials*, 10 (11), 2297.

[4] Redolfi Riva, E., Sinibaldi, E., Grillone, A.F., Del Turco, S., Mondini, A., Li, T., Takeoka, S., and Mattoli, V., 2020, Enhanced *in vitro* magnetic cell targeting of doxorubicin-loaded magnetic liposomes for localized cancer therapy, *Nanomaterials*, 10 (11), 2104.

[5] Iglesias, C.A.M., de Araújo, J.C.R., Xavier, J., Anders, R.L., de Araújo, J.M., da Silva, R.B., Soares, J.M., Brito, E.L., Streck, L., Fonseca, J.L.C., Plá Cid, C.C., Gamino, M., Silva, E.F., Chesman, C., Correa, M.A., de Medeiros, S.N., and Bohn, F., 2021, Magnetic nanoparticles hyperthermia in a non-adiabatic and radiating process, *Sci. Rep.*, 11 (1), 11867.

[6] Bai, S., Hou, S., Chen, T., Ma, X., Gao, C., and Wu, A., 2024, Magnetic nanoparticle-mediated hyperthermia: From heating mechanisms to cancer theranostics, *Innovation Mater.*, 2 (1), 100051.

[7] Gavilán, H., Avugadda, S.K., Fernández-Cabada, T., Soni, N., Cassani, M., Mai, B.T., Chantrell, R., and Pellegrino, T., 2021, Magnetic nanoparticles and clusters for magnetic hyperthermia: Optimizing their heat performance and developing combinatorial therapies to tackle cancer, *Chem. Soc. Rev.*, 50 (20), 11614–11667.

[8] Silveira, M.L.D.C., Silva, I.M.B., and Magdalena, A.G., 2021, Synthesis and characterization of Fe_3O_4-NH_2 and Fe_3O_4-NH_2-chitosan nanoparticles, *Cerâmica*, 67, 295–300.

[9] Zheltova, V., Vlasova, A., Bobrysheva, N., Abdullin, I., Semenov, V., Osmolowsky, M., Voznesenskiy, M., and Osmolovskaya, O., 2020, Fe_3O_4@HAp core–shell nanoparticles as MRI contrast agent: Synthesis, characterization and theoretical and experimental study of shell impact on magnetic properties, *Appl. Surf. Sci.*, 531, 147352.

[10] Zhang, L., Xu, H., Cheng, Z., Wei, Y., Sun, R., Liang, Z., Hu, Y., Zhao, L., Lian, X., Li, X., and Huang, D., 2021, Human cancer cell membrane-cloaked Fe_3O_4 nanocubes for homologous targeting improvement, *J. Phys. Chem. B*, 125 (27), 7417–7426.

[11] Schütz, M.B., Renner, A.M., Ilyas, S., Lê, K., Guliyev, M., Krapf, P., Neumaier, B., and Mathur, S., 2021, ^{18}F-Labeled magnetic nanovectors for bimodal cellular imaging, *Biomater. Sci.*, 9 (13), 4717–4727.

[12] Mylkie, K., Nowak, P., Rybczynski, P., and Ziegler-Borowska, M., 2021, Polymer-coated magnetite nanoparticles for protein immobilization, *Materials*, 14 (2), 248.

[13] Sharma, A., Cornejo, C., Mihalic, J., Geyh, A., Bordelon, D.E., Korangath, P., Westphal, F., Gruettner, C., and Ivkov, R., 2018, Physical characterization and *in vivo* organ distribution of coated iron oxide nanoparticles, *Sci. Rep.*, 8 (1), 4916.

[14] Albutt, N., Sonsupup, S., Sinprachim, T., and Thonglor, P., 2024, Synthesis of magnetic nanoparticles coated with chitosan for biomedical applications, *Key Eng. Mater.*, 1005, 49–57.

[15] Vdoviaková, K., Jenca, A., Jenca, A., Danko, J., Kresáková, L., Simaiová, V., Reichel, P., Rusnák, P., Pribula, J., Vrzgula, M., Askin, S.J., Giretová, M., Briancin, J., and Medvecký, L., 2023, Regenerative potential of hydroxyapatite-based ceramic biomaterial on mandibular cortical bone: An *in vivo* study, *Biomedicines*, 11 (3), 877.

[16] Mo, X., Zhang, D., Liu, K., Zhao, X., Li, X., and Wang, W., 2023, Nano-hydroxyapatite composite scaffolds loaded with bioactive factors and drugs for bone tissue engineering, *Int. J. Mol. Sci.*, 24 (2), 1291.

[17] Ghazagh, P., and Frounchi, M., 2024, Hydroxyapatite/alginate/polyvinyl alcohol/agar composite double-network hydrogels as injectable drug delivery microspheres, *Chem. Pap.*, 78 (5), 2967–2976.

[18] Nikolova, M.P., and Chavali, M.S., 2020, Metal oxide nanoparticles as biomedical materials, *Biomimetics*, 5 (2), 27.

[19] Roudsari, S., Rad-Moghadam, K., and Hosseinjani-

Pirdehi, H., 2019, Dual complex of amylose with iodine and magnetite nano-crystallites: Enhanced superparamagnetic and catalytic performance for synthesis of spiro-oxindoles, *Appl. Organomet. Chem.*, 33 (8), e4993.

[20] Hu, Y., Wang, Q., Chen, S., Xu, Z., Miao, M., and Zhang, D., 2020, Flexible supercapacitors fabricated by growing porous $NiCo_2O_4$ *in situ* on a carbon nanotube film using a hyperbranched polymer template, *ACS Appl. Energy Mater.*, 3 (4), 4043–4050.

[21] Puthumana, G., and Rahul, M.S., 2014, An investigation on finishing technique using abrasives in the presence of a magnetic field, *JMS*, 1 (4), 1–7.

[22] Qiu, G., Guo, Y., Xu, J., Jia, W., Guo, S., Wang, H., Guo, F., and Wu, J., 2022, Hierarchical porous carbon derived from recycled bamboo waste as supercapacitors electrodes based on $FeCl_3$-catalyzed hydrothermal pretreatment: Pore regulation and high-performance analysis, *Int. J. Energy Res.*, 46 (15), 22971–22990.

[23] Fadli, A., Amri, A., Iwantono, I., Adnan, A., Sunarno, S., Sukoco, S., and Mayangsari, M., 2020, The oriented attachment model applied on crystal growth of hydrothermal derived magnetite nanoparticles, *Indones. J. Chem.*, 20 (2), 379–385.

[24] Liu, M.L., Chen, H.F., Li, H.J., Cai, Z.Y., and Ding, J., 2019, Hydrothermal synthesis of $Co(OH)_2$ microspheres, *Solid State Phenom.*, 298, 121–127.

[25] Fadli, A., Amri, A., Sari, E.O., and Adnan, A., 2017, Crystal-growth kinetics of magnetite (Fe_3O_4) nanoparticles using the Ostwald ripening model, *Int. J. Technol.*, 8 (8), 291–319.

[26] Wang, Y., Bai, J., Zuo, J., Peng, H., Hou, H., Wang, H., and Lan, N., 2023, Hydrothermal preparation of cubic sodium zirconium phosphate crystals, *J. Phys.: Conf. Ser.*, 2539 (1), 012048.

[27] Zhang, B., Hu, R., Sun, D., Wu, T., and Li, Y., 2018, Fabrication of magnetite-graphene oxide/MgAl-layered double hydroxide composites for efficient removal of emulsified oils from various oil-in-water emulsions, *J. Chem. Eng. Data*, 63 (12), 4689–4702.

[28] Alamgholiloo, H., Rostamnia, S., Zhang, K., Lee, T.H., Lee, Y.S., Varma, R.S., Jang, H.W., and Shokouhimehr, M., 2020, Boosting aerobic oxidation of alcohols via synergistic effect between TEMPO and a composite Fe_3O_4/Cu-BDC/GO nanocatalyst, *ACS Omega*, 5 (10), 5182–5191.

[29] Azadi, G., Kazemi, F., and Firouzeh, E., 2021, Visible-light-driven photocatalytic Suzuki–Miyaura coupling reaction using novel retrievable magnetic photocatalyst, *ChemistrySelect*, 6 (4), 630–639.

[30] Raso, R., García, L., Ruiz, J., Oliva, M., and Arauzo, J., 2020, Study of Ni/Al-Fe catalyst stability in the aqueous phase hydrogenolysis of glycerol, *Catalysts*, 10 (12), 1482.

[31] Hanasaki, M., Nagata, F., Miyajima, T., and Kato, K., 2018, Controlling particle size of poly(lactic acid)/hydroxyapatite nanoparticles, *Trans. Mater. Res. Soc. Jpn.*, 43 (3), 135–138.

[32] Mehta, M., Bui, T.A., Yang, X., Aksoy, Y., Goldys, E.M., and Deng, W., 2023, Lipid-based nanoparticles for drug/gene delivery: An overview of the production techniques and difficulties encountered in their industrial development, *ACS Mater. Au*, 3 (6), 600–619.

[33] Patel, P., Garala, K., Singh, S., Prajapati, B.G., and Chittasupho, C., 2024, Lipid-based nanoparticles in delivering bioactive compounds for improving therapeutic efficacy, *Pharmaceuticals*, 17 (3), 329.

[34] Tripathi, A.D., Labh, Y., Katiyar, S., Singh, A.K., Chaturvedi, V.K., and Mishra, A., 2024, Folate-mediated targeting and controlled release: PLGA-encapsulated mesoporous silica nanoparticles delivering capecitabine to pancreatic tumor, *ACS Appl. Bio Mater.*, 7 (12), 7838–7851.

[35] Ramirez, P.D., Lee, C., Fedderwitz, R., Clavijo, A.R., Barbosa, D.P.P., Julliot, M., Vaz-Ramos, J., Begin, D., Le Calvé, S., Zaloszyc, A., Choquet, P., Soler, M.A.G., Mertz, M., Kofinas, P., Piao, Y., and Begin-Colin, S., 2023, Phosphate capture enhancement using designed iron oxide-based nanostructures, *Nanomaterials*, 13 (3), 587.

[36] Ajinkya, N., Yu, X., Kaithal, P., Luo, H., Somani, P., and Ramakrishna, S., 2020, Magnetic iron oxide nanoparticle (IONP) synthesis to applications: Present and future, *Materials*, 13 (20), 4644.

[37] Fang, Y., Kim, E., and Strathmann, T.J., 2018, Mineral- and base-catalyzed hydrolysis of organophosphate flame retardants: Potential major fate-controlling sink in soil and aquatic environments, *Environ. Sci. Technol.*, 52 (4), 1997–2006.

[38] Cepan, C., Segneanu, A.E., Grad, O., Mihailescu, M., Cepan, M., and Grozescu, I., 2021, Assessment of the different type of materials used for removing phosphorus from wastewater, *Materials*, 14 (16), 4371.

[39] Zhao, Q., Xing, Y., Liu, Z., Ouyang, J., and Du, C., 2018, Synthesis and characterization of modified BiOCl and their application in adsorption of low-concentration dyes from aqueous solution, *Nanoscale Res. Lett.*, 13 (1), 69.

[40] Ganapathe, L.S., Mohamed, M.A., Mohamad Yunus, R., and Berhanuddin, D.D., 2020, Magnetite (Fe_3O_4) nanoparticles in biomedical application: From synthesis to surface functionalization, *Magnetochemistry*, 6 (4), 68.

[41] Garskaite, E., Stoll, S.L., Forsberg, F., Lycksam, H., Stankeviciute, Z., Kareiva, A., Quintana, A., Jensen, C.J., Liu, K., and Sandberg, D., 2021, The accessibility of the cell wall in Scots pine (*Pinus sylvestris* L.) sapwood to colloidal Fe_3O_4 nanoparticles, *ACS Omega*, 6 (33), 21719–21729.

[42] Yu, J., Xiao, T., Wang, X., Zhou, X., Wang, X., Peng, L., Zhao, Y., Wang, J., Chen, J., Yin, H., and Wu, W., 2019, A controllability investigation of magnetic properties for FePt alloy nanocomposite thin films, *Nanomaterials*, 9 (1), 53.